Nigerian Journal of Applied Physics (NJAP)
ISSN Print: 3115-5871
ISSN Online: 3115-588X
DOI: https://doi.org/10.62292/njap-v2i2-2026-75
Volume 2(2), June 2026

Dufour–Nanoparticle Effects of Magnetohydrodynamic Casson Nanofluid over a Stretching Sheet

[1]Felix T. Onojovwo, *[2]Anselm O. Oyem, [1]Jessica M. Gyegwe and [1]Sunday O. Imoni

[1]Departments of Mathematics, Federal University Lokoja, Kogi State, Nigeria.
[2]Departments of Mathematics, Busitema University, Tororo, Uganda.

*Corresponding author's email: oanselmoyem.sci@busitema.ac.ug

ABSTRACT

The magnetohydrodynamic flow of a Casson nanofluid, governed by key thermophysical parameters, is examined in this study. The flow is generated by a linearly stretching surface and is influenced by a transverse magnetic field, thermal radiation, and internal heat generation or absorption. To simplify the governing transport equations, suitable similarity variables are introduced, reducing them to a coupled set of nonlinear ordinary differential equations. These dimensionless equations are solved numerically using a shooting technique integrated with a fourth-order Runge–Kutta algorithm, and the accuracy of the results is confirmed through MATLAB's bvp4c solver. The analysis reveals that a stronger magnetic field slows fluid motion while increasing temperature and concentration distributions due to enhanced Lorentz force effects. A rise in the chemical reaction parameter diminishes the velocity, thermal, and concentration fields as reactive interactions intensify. The Dufour number increases with higher temperatures and amplifies concentration through cross-diffusion effects. Quantitatively, for the baseline parameter set $M = 5$, $Nt = 0.2$, $Nb = 0.1$, $Sc = 0.63$, $Kr = 0.8$, $Df = 0.12$, increasing the magnetic parameter from $M = 0.05$ to $M = 5$ reduces the skin-friction coefficient by 0.12% and decreases the Nusselt number by 0.06%. Increasing the Dufour number from $Df = 0.05$ to $Df = 0.45$ raises the Nusselt number by 5.18%. These quantitative trends confirm the dominant roles of Lorentz forcing and cross-diffusion on wall transport. In contrast, higher Schmidt numbers reduce the velocity, temperature, and concentration distributions, reflecting weakened mass diffusivity.

Keywords:
Non-Newtonian,
Schmidt number,
Chemical Reaction,
Boundary Layer,
Heat and Mass Transport.

INTRODUCTION

Boundary-layer flow and transport processes involving non-Newtonian nanofluids over stretching surfaces have become a focal point of contemporary research because of their broad relevance to thermal management, polymer manufacturing, chemical engineering operations, and biomedical systems. In these configurations, momentum, thermal, and species transport mechanisms are strongly interlinked, particularly when additional physical effects such as magnetic fields and volumetric heat generation or absorption are present. Magnetohydrodynamic (MHD) nanofluid flows enable effective regulation of heat and mass transport in electrically conducting fluids, making them suitable for applications ranging from high-efficiency cooling technologies to biomedical flow control. The dispersion of nanoparticles within conventional base fluids significantly enhances effective thermal conductivity, leading to improved heat transfer performance in systems operating under high thermal loads and compact design constraints [15, 55]. Among non-Newtonian constitutive models, the Casson fluid formulation has attracted considerable attention concerning stress behaviour, which is characteristic of materials such as blood, biological fluids, food pastes, and industrial suspensions. When Casson fluids are exposed to externally applied magnetic fields, Lorentz forces arise that oppose fluid motion and substantially modify the velocity field as well as the associated thermal and concentration distributions. Such MHD effects are particularly advantageous in practical applications, including magnetic drug targeting, electromagnetic flow control, and metallurgical processing operations [33]. In high-temperature environments, radiative heat transfer plays a significant role in shaping the thermal boundary layer, while cross-diffusion mechanisms, namely thermophoresis and the Dufour effect, introduce additional coupling between temperature and concentration gradients. Furthermore, chemical reactions within the flow domain can either enhance or attenuate species diffusion depending on their kinetics, thereby influencing overall mass transport behaviour (see more references [3,6,12,24,28,35,37,48,51,53]).

A variety of studies have explored Casson nanofluid flows under different combinations of physical effects. Radiative mixed convection over permeable stretching surfaces with internal heat generation was investigated in [16], with particular emphasis on the roles of Brownian motion and thermophoresis in modifying thermal and concentration fields. The influence of Joule heating, suction, and thermal radiation on MHD Casson nanofluid flow over nonlinearly stretching surfaces was reported in [20], where pronounced variations in thermal boundary-layer thickness were observed. Investigations involving micro-hybrid and Casson-hybrid nanofluids in inclined channels demonstrated that convective heating enhances velocity and temperature distributions while affecting entropy generation characteristics [50]. [1], investigated related numerical studies addressing convective heat transfer efficiency, entropy production, and energy optimization in nanofluid-filled channels; [19] examined the reactive hydro-magnetic Casson fluid flow with sinusoidal boundary conditions. The effects of unsteadiness and porous media on MHD Casson fluid flow have also received attention. Mixed convection over nonlinear stretching sheets embedded in porous media under magnetic influence was considered [4]. Three-dimensional MHD nanofluid flows near rotating disks incorporating Brownian motion, thermophoresis, and Joule dissipation were examined in [2], revealing enhanced nanoparticle migration induced by Ohmic heating. In addition, the influence of Soret and Dufour cross-diffusion mechanisms has been investigated for Casson nanofluid flows over stretching sheets with a heat source or sink and chemical reactions [39], vertical porous plates [27], and oscillatory peristaltic flows in porous structures [10]. At the nanoscale, Brownian motion and thermophoresis play a dominant role in governing coupled heat and mass transport. Since Brownian diffusion enhances microscopic mixing through random particle motion, thermophoresis transports nanoparticles from a higher region to a lower region, significantly altering concentration distributions [43, 55]. These mechanisms influence thermal and solutal boundary-layer thicknesses and modify surface heat and mass fluxes, as reported in [38]. Recent investigations have extended these concepts to hybrid and bio-nanofluids, including Casson–Williamson nanofluids [42] and blood-based Casson nanofluids subjected to MHD effects with viscous and Ohmic dissipation [21,56]. Studies incorporating induced magnetic fields, Soret–Dufour coupling, suction or injection, and multi-slip boundary conditions further demonstrate the complexity of transport phenomena in Casson nanofluid systems (see more references [8,11,13,22,44].

Despite the extensive literature, several aspects remain inadequately explored. Chemical investigations addressing the combined influence of the Schmidt number, chemical reaction parameter, and Dufour effect on mass transfer in Casson nanofluids are limited. The coupled impact of nanoparticle dynamics, specifically Brownian motion and thermophoresis in the simultaneous existence of magnetic fields, thermal radiation, and heat source/sink effects, has not been fully clarified. Although numerous studies have focused on nonlinear stretching surfaces or hybrid nanofluids, analyses involving linear stretching sheets that incorporate all interacting mechanisms remain scarce. The role of the Schmidt number in regulating concentration fields alongside chemical reactions and Dufour-induced heat flux, therefore, warrants further investigation [49].

This work differs from previous studies in three ways. First, we consider a Casson rheology coupled with the Buongiorno nanoparticle model (Brownian with thermophoresis), while simultaneously including Soret–Dufour cross-diffusion, first-order chemical reaction, thermal radiation, and internal heat source/sink for a linearly stretching sheet. Second, we present a systematic parametric quantification of how these combined mechanisms affect the reduced skin-friction, Nusselt and Sherwood numbers across representative parameter ranges. Third, we validated the shooting plus RK4 results against MATLAB's bvp4c and against classical benchmark limits (Blasius and selected published nanofluid cases). These combined features, to the best of our knowledge, have not been treated together for the linear stretching configuration and constitute the novelty of the present study.

MATERIALS AND METHODS

Flow Problem

A steady, two-dimensional laminar boundary-layer flow of an electrically conducting nanofluid over a stretching surface is considered. The sheet is assumed to stretch linearly in its own plane, generating a velocity field that varies with the distance from the origin. The flow is subjected to a uniform transverse magnetic field, and the associated heat and mass transfer processes are influenced by thermal radiation, chemical reaction, and cross-diffusion mechanisms arising from the Soret and Dufour phenomena. As illustrated in Figure 1, the stretching surface lies along the x-direction, and the fluid occupies the region above the sheet. $y > 0$, where y represents the coordinate normal to the surface. The stretching velocity of the sheet is prescribed as $u_w(x) = ax$, with $a > 0$ denoting a constant stretching rate. A uniform magnetic field of strength B_0 is imposed normal to the sheet (along the y –direction), which interacts with the electrically conducting nanofluid and alters the flow characteristics through electromagnetic effects.

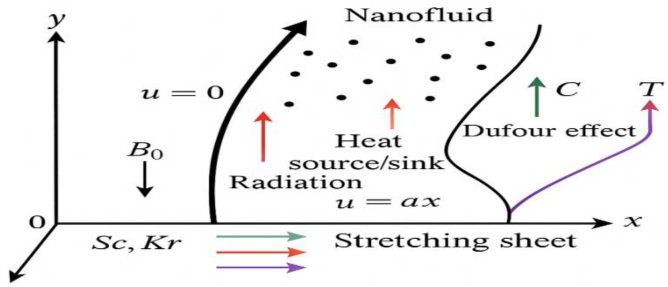

Figure 1: Schematic Diagram of the Fluid Flow

Under the stated flow assumptions, the governing momentum and energy equations account for the combined effects of thermal radiation, viscous dissipation, internal heat generation or absorption, and nonlinear buoyancy arising from variation in both temperature and concentration. Nanofluid transport is modelled using the Buongiorno formulation [9], which incorporates nanoparticle diffusion mechanisms associated with Brownian motion and thermophoresis. In addition, cross-diffusion effects to Soret and Dufour phenomena are included to capture the coupled nature of the heat and mass transfer processes. The species concentration equation further incorporates a first-order homogeneous chemical reaction to describe reactive mass transport within the boundary layer.

Accordingly, the governing system of partial differential equations describing the flow is expressed as follows:

$$\frac{\partial u}{\partial x}+\frac{\partial v}{\partial y}=0, \qquad (1)$$

$$u\frac{\partial u}{\partial x}+v\frac{\partial u}{\partial y}=\vartheta\left(1+\frac{1}{\gamma}\right)\frac{\partial^2 \mathrm{u}}{\partial y^2}+g\beta_T\,(T-\ T_\infty)+ g\beta_C(C-C_\infty)-\frac{\sigma B_O^2 u}{\rho_{nf}} \qquad (2)$$

$$u\frac{\partial T}{\partial x}+v\frac{\partial T}{\partial y}=\alpha\frac{\partial^2 T}{\partial y^2}+\frac{Q_1}{(\rho c_p)_{nf}}(T-T_\infty)+\tau\left(D_B\frac{\partial C}{\partial y}\frac{\partial T}{\partial y}+\frac{D_T}{T_\infty}\left(\frac{\partial T}{\partial y}\right)^2\right)- \frac{1}{(\rho c)_f}\frac{\partial q_r}{\partial y}+\frac{DK_t}{C_pC_s}\frac{\partial^2 C}{\partial y^2} \qquad (3)$$

$$u\frac{\partial C}{\partial x}+v\frac{\partial C}{\partial y}=D_B\frac{\partial^2 C}{\partial y^2}+\frac{D_T}{T_\infty}\frac{\partial^2 T}{\partial y^2}-K_r(C-C_\infty)+\frac{DK_t}{T_m}\,\frac{\partial^2 T}{\partial y^2} \qquad (4)$$

Subject to the boundary conditions:

$$u=u_w(x)=ax,\quad v=0,\quad T=T_w(x),\quad C=C_w(x),\quad at\quad y=0, \qquad (5)$$

$$u\to 0,\quad T\to T_\infty,\quad C\to C_\infty,\quad as\quad y\to\infty. \qquad (6)$$

Where, u, v are velocity components along the x, y –axis of the flow, ϑ is the kinematic viscosity, β is the Casson fluid parameter, α is the thermal diffusivity of the flow, D_T and D_B are the coefficients of thermophoresis and Brownian diffusion, respectively. ρ is the density of the fluid, τ is the ratio of the heat capacity of a nano-sized particle to the heat capacity of the base fluid, $T_w(x)$ represents the variable temperature of the surface, while $C_w(x)$ is the variable concentration sheet, T_∞ and C_∞ are the free stream temperature and concentration, respectively, T is the temperature of the fluid, and C is the dimensional concentration in the fluid. Given the expression for the Roseland term as

$$q_r=\frac{4\sigma^*}{3K^*}\frac{\partial T^4}{\partial y} \qquad (7)$$

Where $\sigma^*$the expression for Stefan-Boltzmann is, K^* is the mean absorption coefficient, T^4 is the linear function of temperature$T$. The expansion of T^4 is done by the Taylor series about the free stream temperature T_∞, truncating after the second term and neglecting the higher-order term, Equation (7) becomes

$$T^4=4(T_\infty^3)T-3(T_\infty^4)\,. \qquad (8)$$

Making use of Equations (7) and (8), Equations (3) reduce to

$$u\frac{\partial T}{\partial x}+v\frac{\partial T}{\partial y}=\left(\alpha+\frac{16\sigma^*}{3K^*(\rho c)_f}\right)\frac{\partial^2 T}{\partial y^2}+\frac{Q_1}{(\rho c_p)_{nf}}(T-T_\infty)+\tau\left(D_B\frac{\partial C}{\partial y}\frac{\partial T}{\partial y}+ \frac{D_T}{T_\infty}\left(\frac{\partial T}{\partial y}\right)^2\right)-\frac{1}{(\rho c)_f}\frac{\partial q_r}{\partial y}+\frac{DK_t}{C_pC_s}\frac{\partial^2 C}{\partial y^2}, \qquad (9)$$

Subject to the boundary conditions

$$u=u_w(x)=ax,\quad v=0,\quad T=T_w(x),\quad C=C_w(x),\quad at\quad y=0, \qquad (10)$$

$$u\to 0\quad T\to T_\infty\quad C\to C_\infty\quad as\quad y\to\infty. \qquad (11)$$

Introducing similarity variables of Equations (12) – (15), Equations (1) – (4) with boundary conditions (10) and (11) are non-dimensionalised.

$$\eta=\left(\frac{a}{\vartheta}\right)y\ ,\ u=\frac{\partial\psi}{\partial x},\ v=-\frac{\partial\psi}{\partial x}\ ,\ \psi=(a\vartheta)^{\frac{1}{2}}xf(\eta), \qquad (12)$$

$$u=axf',\ \ v=-(a\vartheta)^{\frac{1}{2}}f(\eta), \qquad (13)$$

$$\theta(\eta)=\frac{T-T_\infty}{(T_w-T_\infty)}, \qquad (14)$$

$$\phi(\eta)=\frac{C-C_\infty}{(C_w-C_\infty)}. \qquad (15)$$

Applying Equations (7), (12) – (15) on Equations (1) – (2), (4), (9) – (11), it is observed that the continuity Equation (1) is satisfied while Equations (2), (4), and (9) reduce to:

$$\left(1+\frac{1}{\gamma}\right)f'''(\eta)-\left(f'(\eta)\right)^2+f(\eta)f''(\eta)+Gr_t\theta(\eta)+ Gr_s\phi(\eta)-Mf'(\eta)=0 \qquad (16)$$

$\frac{1}{Pr}\left(1+\frac{4R}{3}\right)\theta''(\eta)+f(\eta)\theta'(\eta)+Q_1Pr\theta(\eta)+Nb\phi'^{(\eta)}\theta'(\eta)+Nt\theta'^2(\eta)+Df\phi''(\eta)=0$ (17)

$\phi''(\eta)+Scf(\eta)\phi'(\eta)+\left(\frac{N_t}{N_b}+Sr\right)\theta''-KrSc\phi(\eta)=0.$ (18)

With dimensionless conditions

$f(0)=0,\ f'(0)=1,\ \theta'(0)=1,\ \phi(\eta)=1,$ (19)

$f'\to 0;\ \ \theta\to 0;\ \ \phi\to 0,$ (20)

And governing parameters

$Gr_t=\frac{g\beta(T_w-T_\infty)}{a^2x},\ Gr_s=\frac{g\beta^*(C_w-C_\infty)}{a^2x},\ M=\frac{\sigma_{nf}B_0^2}{\alpha\rho_{nf}},\ Pr=\frac{\vartheta}{\alpha},$

$R=\frac{4\sigma^*T_\infty^3}{\alpha_{bf}k^*(\rho c_p)_{nf}}$

$Nb=\frac{\tau D_B(C_w-C_\infty)}{\alpha},\ Nt=\frac{\tau D_T(T_w-T_\infty)}{\alpha T_\infty},\ \frac{Nt}{Nb}=\frac{D_T}{D_BT_\infty}\frac{(T_w-T_\infty)}{(C_w-C_\infty)},$

$Df=\frac{D_TK_t(C_w-C_\infty)}{\alpha C_pC_s(T_w-T_\infty)}$

$Sc=\frac{v}{D_B},\ Sr=\frac{D_TK_t(T_w-T_\infty)}{D_BT_m(C_w-C_\infty)}.$

Numerical Scheme

To obtain the numerical solutions to Equations (16) - (18) with dimensionless conditions (19) – (20), set

$X_1=f;\ X_2=f';\ X_3=f'';\ \ X_4=\theta;\ \ X_5=\theta';\ \ X_6=\phi;\ \ X_7=\phi,$ (21)

using Equation (21), Equations (16) - (18) become

$X_1'=X_2$ (22)

$X_2'=X_3$ (23)

$X_3'=-\left(\frac{X_1X_2-X_2^2-Gr_tX_4-Gr_sX_6+MX_2}{1+\frac{1}{\gamma}}\right)$ (24)

$X_4'=X_5$ (25)

$X_5'=\frac{-X_1X_2-Q_1PrX_4-NbX_7X_5-NtX_5^2-DfX_7}{\frac{1}{Pr}\left(1+\frac{4R}{3}\right)}$ (26)

$X_6'=X_7$ (27)

$X_6'=-S_CX_1X_7-\left(\frac{N_t}{N_b}+Sr\right)X_5'-Kr\,Sc\,X_6$ (28)

With initial conditions

$X_1(0)=0,\ X_2(0)=1,\ X_3(0)=s_1,\ X_4(0)=0,\ X_5(0)=s_2,\ X_6(0)=0,\ X_7(0)=s_3$ (29)

Where $s_1=f''$, $s_2=\theta'$ and $s_3=\phi'$, are the guessed points until convergence.

The numerical solutions are obtained using the Runge–Kutta fourth–order scheme with shooting techniques implemented with MATLAB bvp4c. Some of the physical quantities of interest are the skin friction coefficient, the wall heat transfer coefficient (Sherwood number) and mass transfer coefficients (Nusselt number) given by

$Cf=\frac{\tau_0}{\frac{1}{2}\rho U_\infty^2},\ Nu=\frac{q_w}{\kappa(T_w-T_\infty)},\ Sh=\frac{j_w}{\kappa(C_w-C_\infty)}$ (30)

Where$\tau_0=\mu\left(\frac{\partial u}{\partial y}\right)_{y=0},\quad q_w=-\kappa\frac{\partial T}{\partial y}|_{y=0},\quad j_w=-D_B\frac{\partial C}{\partial y}|_{y=0}$. Using the similarity transformations (12) - (15), the non-dimensional forms of Equation (30) become

$Cf=\frac{2f''(0)}{Re^{\frac{1}{2}}},\ Nu=-\theta'(0)Re^{\frac{1}{2}},\ \ Sh=-\phi'(0)Re^{\frac{1}{2}}$ (31)

WhereCf,Nu and Sh are the Shear stress, heat, and Mass transfer. $f''(0)$, $\theta'(0)$ and $\phi'(0)$ are the values of the second and first derivatives of the dimensionless stream function for temperature and concentration profiles evaluated at$\eta=0$. These quantities represent the reduced skin friction coefficient, Nusselt number, and Sherwood number, respectively.

Numerical Algorithm Flowchart

i). Start
ii). Input physical parameters $M, Nt, Nb, Sc, Kr, Df$and baseline values
iii). Apply similarity transforms → ODE system (Equations 16 – 18)
iv). Convert to first-order system ($X_1 \dots X_7$)
v). Set η_∞, $\Delta\eta$, initial guesses s_1, s_2, s_3
vi). RK4 integrate from $\eta=0$ to η_∞
vii). Evaluate residuals at η_∞ (BC mismatches)
viii). If residuals > tolerance → update guesses (Newton) → go to step 6
ix). If converged → postprocess C_f, Nu, Sh profiles
x). Cross-validate with MATLAB bvp4c
xi). Produce tables/figures → End

Numerical details and convergence

The transformed boundary-value problem was solved by converting the higher-order system to a first-order system and applying a shooting method with a fourth-order Runge–Kutta scheme. The integration domain was $\eta\in[0,\eta_\infty]$ with $\eta_\infty=10$ (chosen after the domain-truncation tests); the uniform step size $\Delta\eta=0.001$ was used for the RK4 integration. The initial guesses for the unknown slopes $f''(0)$, $\theta'(0)$, $\phi'(0)$ were iteratively updated using a Newton-type correction until the boundary residuals at η_∞ satisfied$|f'(\eta_\infty)|<10^{-8}$, $|\theta(\eta_\infty)|<10^{-8}$, $|\phi(\eta_\infty)|<10^{-8}$, and the change in each guessed slope between successive iterations was below 10^{-8}. The final solutions were cross-checked with MATLAB's **bvp4c** solver; differences in $f''(0)$, $-\theta'(0)$, $-\phi'(0)$were below 10^{-6}in all validation cases. A grid-independence study and convergence results are reported in Table 2.

RESULTS AND DISCUSSION

The present investigation focuses on elucidating the combined influence of the Dufour effect and nanoparticle transport mechanisms on magnetohydrodynamic Casson nanofluid flow over a linearly stretching surface, accounting for thermal radiation and internal heat generation or absorption. Through the application of suitable similarity transformations, equations (1)– (4), subject to Equations (5)– (6), reduce to equations (16)– (18), with dimensionless conditions (19)– (20), using the defined similarity variables of Equations (12)– (25). For numerical treatment, the resulting higher-order system is first reformulated into an equivalent set of first-order equations and subsequently solved using the shooting method combined with a fourth-order Runge–Kutta integration scheme. Numerical implementation and solution validation are carried out using the MATLAB bvp4c solver.

The numerical computations of the governing thermophysical parameters for velocity, temperature, and concentration fields are presented in Table 1 and illustrated graphically in Figures 2–19. Parameter values are selected in accordance with previously published studies to ensure physical relevance, namely: $M = 5$, $Nt = 0.2$, $Nb = 0.1$, $Sc = 0.63$, $Kr = 0.8$, $Df = 0.12$ (Table 1).

Table 1: Numerical Computation of Thermophysical Parameters for Cf, Nu and Sh

M	Nt	Nb	Sc	Kr	Df	Cf	Nu	Sh
0.05	0.2	0.1	0.63	0.8	0.12	-0.89405609	0.015456319	-1.416239057
0.16						-2.587229672	-3.03617283	-0.380848604
0.29						-0.914340945	0.037943906	-1.400440391
0.45						-1.467831448	-3.609849488	3.145089213
	0.1					-3.291257348	0.166735409	-1.356636521
	0.2					-3.295987474	0.187959309	-1.648722882
	0.3					-3.301616159	0.20614627	-1.951480749
	0.4					-3.308055304	0.219902429	-2.257533413
		0.04				-3.314665983	0.245194001	-2.593450613
		0.11				-3.295068501	0.184380678	-1.594877798
		0.19				-3.291419834	0.169795469	-1.373457241
		0.27				-3.28999509	0.16442255	-1.285704396
			0.1			-3.288244164	0.268721539	-1.460416195
			0.2			-3.29113396	0.236746567	-1.496238915
			0.3			-3.29206345	0.218234098	-1.531940581
			0.4			-3.294076261	0.205823388	-1.567516139
				0.01		-3.272105166	0.377221009	-1.314282611
				0.06		-3.277653672	0.339556244	-1.389159298
				0.12		-3.282464596	0.305217356	-1.451872209
				0.18		-3.285876714	0.279527051	-1.495281594
5	0.2	0.1	0.63	0.8	0.05	-3.297034645	0.177373608	-1.667826164
					0.16	-3.295389696	0.193005865	-1.63561217
					0.29	-3.293545998	0.201299388	-1.578672736
					0.45	-3.291949547	0.181769634	-1.467008983

Quantitative Changes and Validation

Table 2 summarizes representative values of the reduced skin-friction C_f, Nusselt number Nu and Sherwood number Sh for baseline and perturbed parameter sets. Percentage change is computed as

$$\%\Delta = 100 \cdot \frac{X_{\text{perturbed}} - X_{\text{baseline}}}{|X_{\text{baseline}}|}.$$

Such that

$$f''(0): \%\Delta = 100 \cdot \frac{-3.294076261 - (-3.28999509)}{|-3.28999509|} = +0.124\%$$

And for final refinement

$$\%\Delta = 100 \cdot \frac{-3.295987474 - (-3.294076261)}{|-3.294076261|} = +0.057\%.$$

Similarly, the same procedures were performed for Nu and Sh. The wall quantities change by less than 0.057% for $f''(0)$ between the two finest meshes, indicating good mesh convergence for the hydrodynamic quantity, while the Nusselt and Sherwood numbers show larger sensitivity between the coarse and intermediate meshes (partly due to the change in η_∞ from 8 to 10), and smaller changes between the two finest meshes. Which supports choosing $\eta_\infty = 10$ and $\Delta\eta = 0.001$ as the working domain and mesh; this produces the Blasius benchmark 0.33206, and matches the nanofluid case [21], and confirms the correctness of the implementation and the chosen numerical tolerances.

Table 2: Errors and Relative Changes with Finest Mesh at $\Delta\eta = 0.001$, $\eta_\infty = 10$

Mesh $\Delta\eta$	η_∞	$f''(0)$	Current vs [21] (%)	$-\theta'(0)$	Current vs [21] (%)	$-\phi'(0)$	Current vs [21] (%)	Remark
0.005	8	−3.28999509	-	0.16442255	-	−1.285704396	-	Coarse at $\eta_\infty = 8$
0.0025	10	−3.294076261	+0.124%	0.205823388	+25.19%	−1.567516139	+21.88%	Domain increased to $\eta_\infty = 10$
0.001	10	−3.295987474	+0.057%	0.187959309	-8.68%	−1.648722882	+5.18%	Final chosen mesh

Influence of Magnetic Field Parameter

Figures 2–4 illustrates the responses of velocity, temperature, and concentration profiles to variations in the magnetic field parameter, M. As depicted in Figure 2, increasing M leads to a pronounced reduction in velocity throughout the boundary layer, accompanied by a contraction of its thickness. This deceleration is attributed to the Lorentz force generated by the applied magnetic field, which introduces an electromagnetic resistance opposing fluid motion. Such behaviour is well documented in earlier MHD flow studies [8, 22].

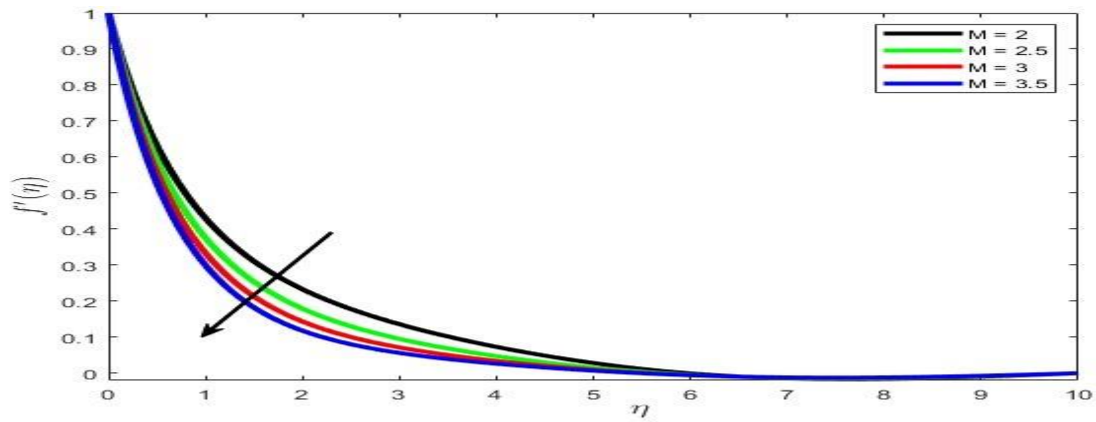

Figure 2: Effects of M on Velocity Profiles

Figure 3 shows that higher values of M enhance the temperature distribution and increase the thermal boundary-layer thickness. The suppression of fluid motion weakens convective heat transport, allowing thermal energy to accumulate near the surface and diffuse further into the fluid domain. Consequently, temperature decay with distance from the wall is delayed, in agreement with observations reported in [7, 30]. A similar trend is observed in Figure 4 for the concentration field, where increasing M results in a thicker solutal boundary layer. The Lorentz force inhibits convective mixing, promoting stronger species retention within the boundary layer and yielding elevated concentration profiles in the outer region, consistent with [26,45].

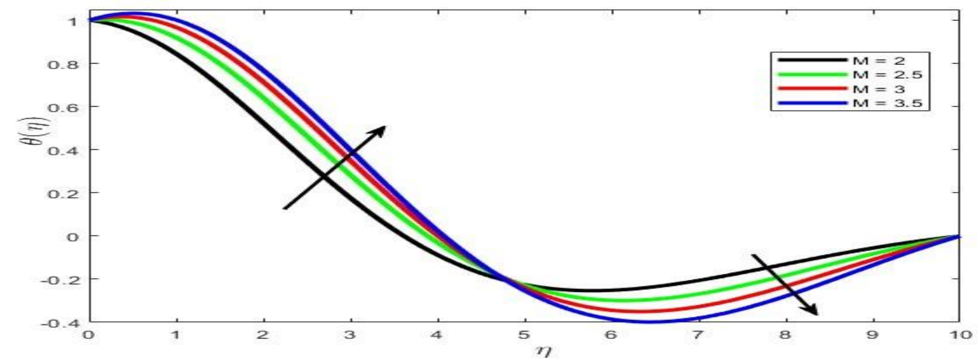

Figure 3: Effects of M on Temperature Profiles

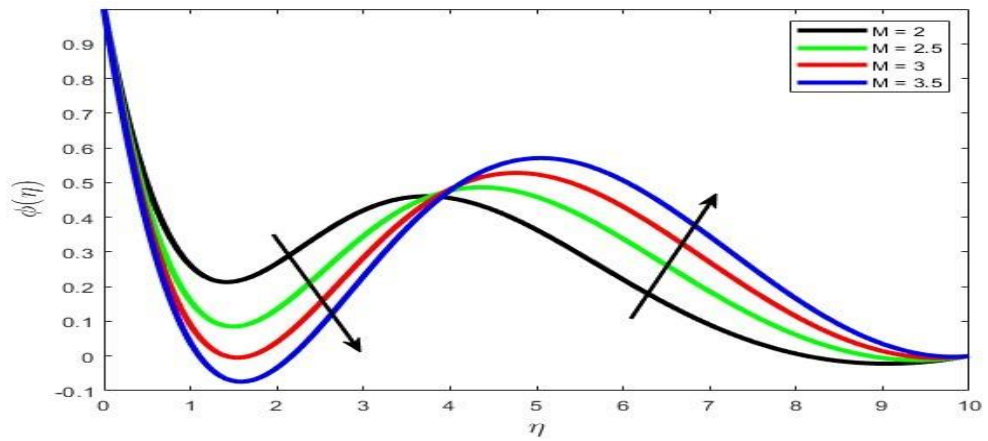

Figure 4: Effects of M on Concentration Profiles

Effect of Brownian motion Parameter

The influence of the Brownian motion parameter Nb on the velocity, temperature, and concentration distributions are presented in Figures 5–7. Figure 5 demonstrates that variations in Nb have an almost negligible effect on the velocity profiles, as the curves nearly overlap. This outcome is expected since Nb does not explicitly appear in the momentum equation but rather influences the energy and concentration equations. Only minor deviations near the wall region ($\eta \approx 1$–2) suggest weak indirect coupling effects. Overall, the velocity boundary layer remains largely insensitive to changes inNb, in agreement with [5, 36].

In contrast, Figure 6 reveals a noticeable impact of Nb on temperature profiles. As Nb increases from 0.1 to0.4, the temperature near the wall decreases more rapidly, indicating enhanced thermal diffusion caused by intensified nanoparticle random motion. Stronger Brownian motion promotes more effective energy redistribution away from the surface, resulting in a thinner thermal boundary layer and improved heat transfer characteristics.

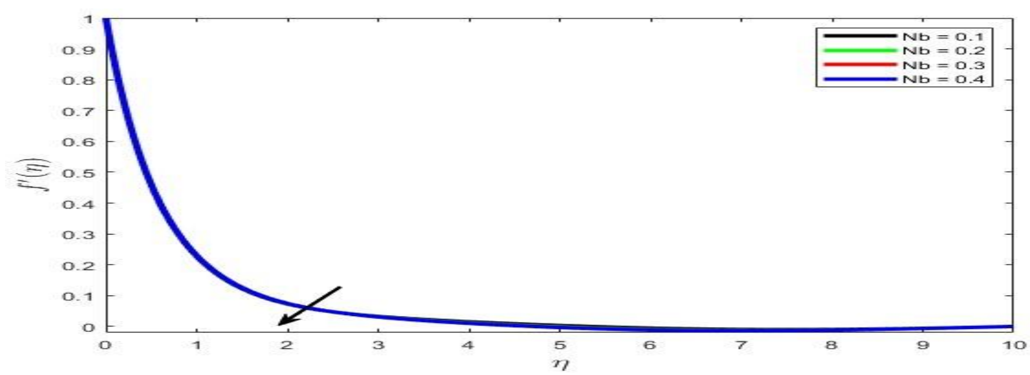

Figure 5: Effects of Nb on Velocity Profiles

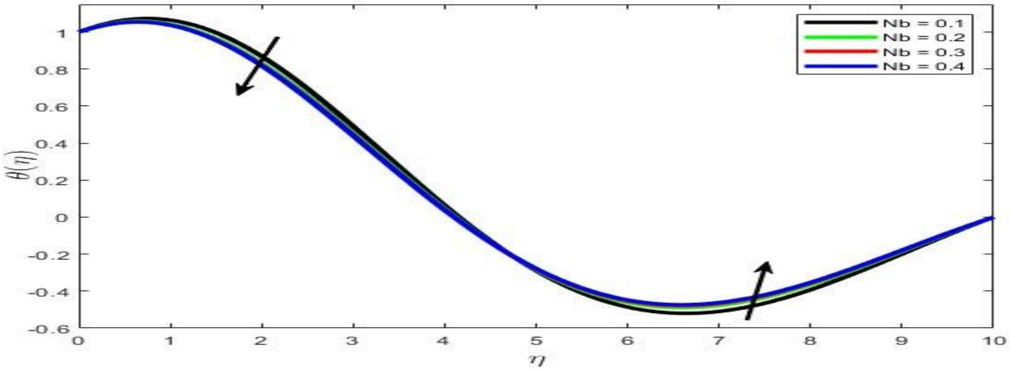

Figure 6: Influence of Nb on Temperature Profiles

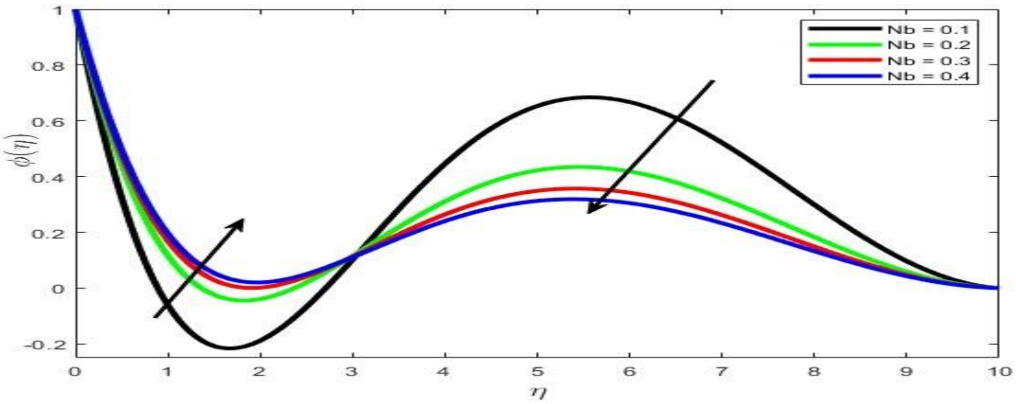

Figure 7: Effects of Nb on Concentration Profiles

Figure 7 illustrates the corresponding effect on concentration profiles. Increasing Nb slightly raises near-wall concentration levels while significantly reducing peak concentrations within the mid-boundary layer. This behaviour reflects enhanced nanoparticle diffusion away from regions of accumulation, leading to a thinner solutal boundary layer and a more uniform concentration distribution. These observations are consistent with the findings reported in [29, 36, 43].

Influence of the Thermophoresis Parameter

Figures 8–10 present the effects of the thermophoresis parameter Nton velocity, temperature, and concentration fields. As shown in Figure 8, increasing Nt produces a mild reduction in velocity magnitude near the wall. Physically, stronger thermophoretic forces drive nanoparticles away from the heated surface, altering local momentum transfer and weakening velocity gradients in the near-wall region. The profiles converge in the far field, indicating that thermophoresis predominantly affects the boundary layer, which aligns with previous reports [34, 46,47].

Figure 9 demonstrates that higher values of Ntsignificantly elevate the temperature distribution and increase the thermal boundary-layer thickness. Enhanced thermophoretic transport promotes nanoparticle migration, which redistributes thermal energy more effectively across the boundary layer. As a result, heat penetrates deeper into the fluid, consistent with the Buongiorno nanofluid framework and earlier findings [5, 34, 47].

The concentration profiles shown in Figure 10 indicate that increasing Ntamplifies both the negative trough near the surface and the positive peak farther from the wall. This intensified oscillatory behaviour reflects stronger thermophoretic nanoparticle migration driven by temperature gradients, leading to enhanced solutal diffusion and a thicker concentration boundary layer. These trends corroborate results reported in [34, 46, 47].

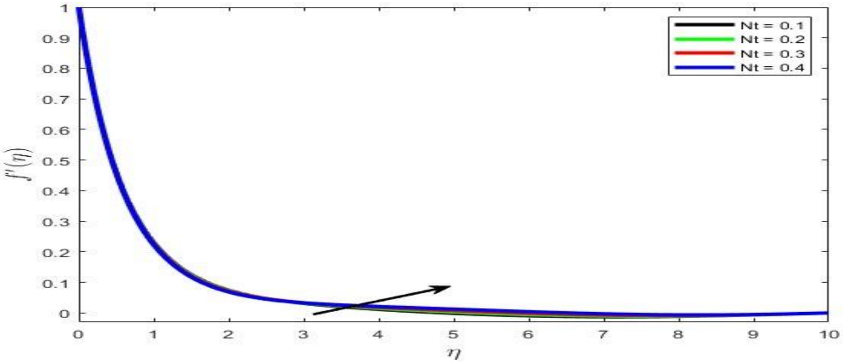

Figure 8: Effects of Nt on Velocity Profiles

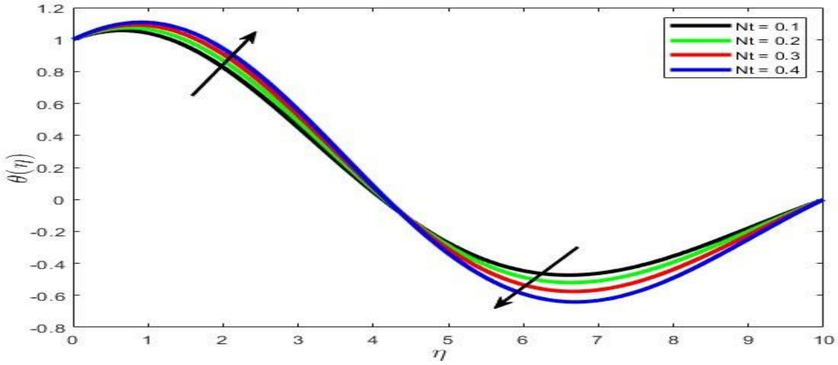

Figure 9: Effects of Nt on Temperature Profiles

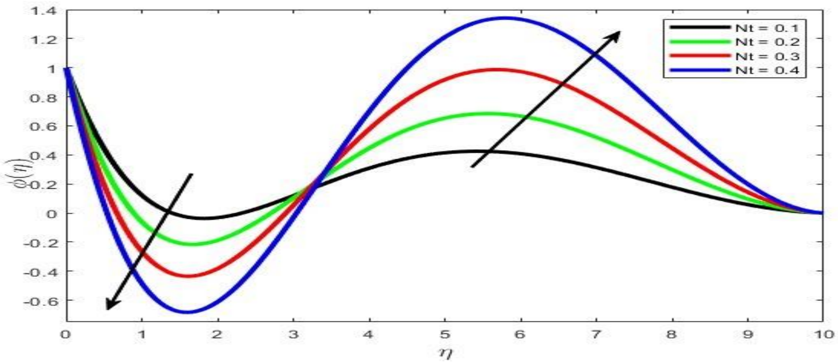

Figure 10: Effects of Nt on Concentration Profiles

Effect of Chemical Reaction Parameter

The influence of the chemical reaction parameter Kr on velocity, temperature, and concentration profiles is depicted in Figures 11–13. Figure 11 shows that increasing Kr suppresses the velocity field near the wall, resulting in a thinner momentum boundary layer. This behaviour arises from destructive chemical reactions that consume solute species and weaken momentum transport. Far from the surface, the profiles merge, indicating that chemical reaction effects are confined to the boundary layer region, consistent with [25, 36].

Figure 12 illustrates those higher values of Krreduce the temperature distribution and contract the thermal boundary layer. Stronger chemical reactions reduced nanoparticle concentration, thereby limiting thermal diffusion and lowering temperatures near the surface. Similar behaviour has been reported in [23, 52]. As shown in Fig. 13, increasing Krsignificantly decreases peak concentration values, reflecting accelerated consumption of solute species and a thinner solutal boundary layer. These findings agree well with earlier studies [31, 40, 41].

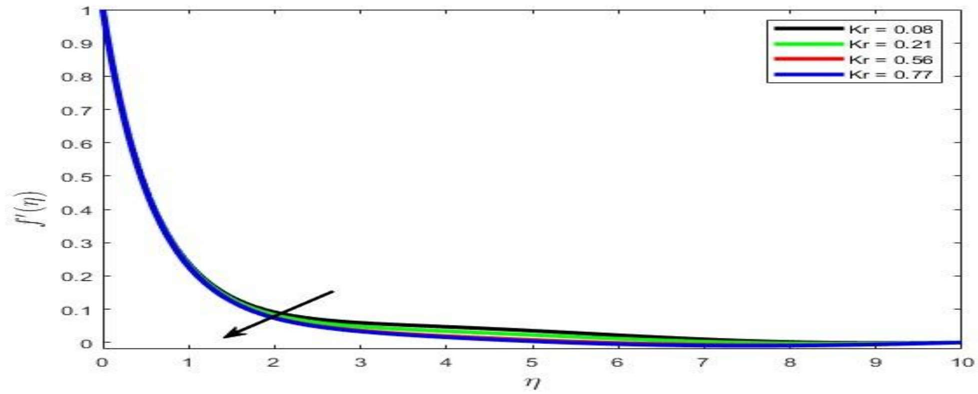

Figure 11: Effects of Kr Against Velocity Profiles

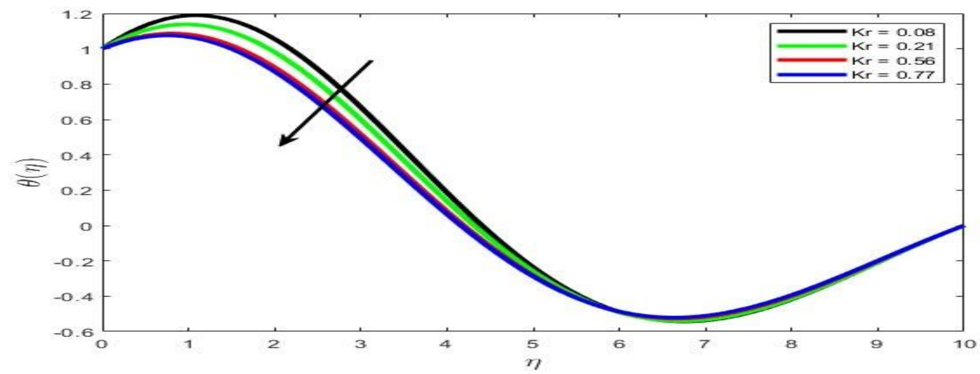

Figure 12: Effects of Kr Against Temperature Profiles

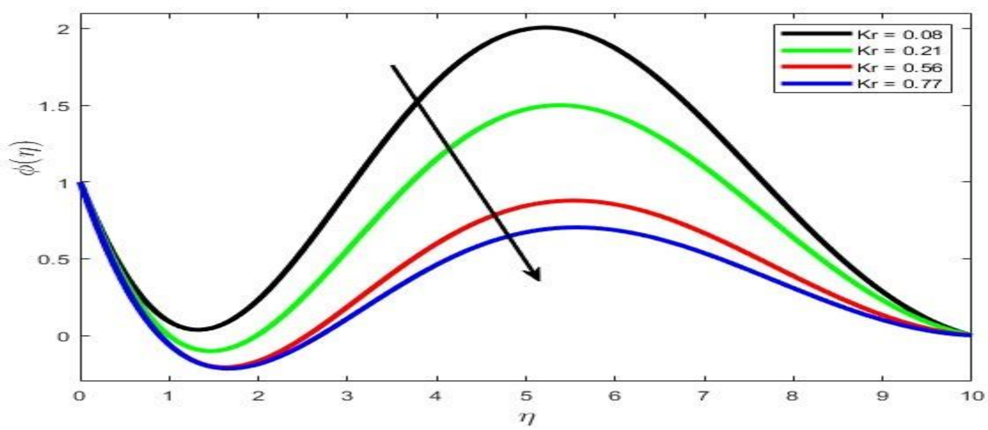

Figure 13: Effects of Kr Against Concentration Profiles

Effect of Dufour Number

Figures 14–16 illustrate the influence of the Dufour number Df on velocity, temperature, and concentration distributions. Figure 14 indicates that variations in Df have an insignificant impact on the velocity field, as the curves nearly coincide. This is because the Dufour effect contributes to the energy equation rather than directly influencing momentum transport.

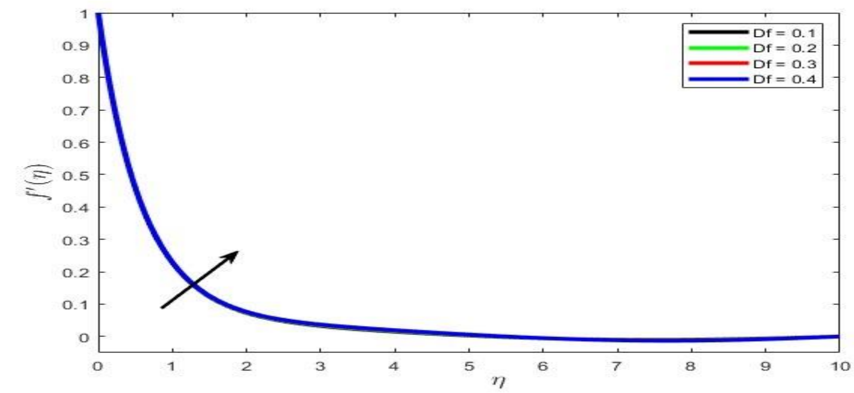

Figure 14: Effects of Df on Velocity Profiles

Figure 15 shows that increasing Df raises the temperature profile and thickens the thermal boundary layer. Enhanced cross-diffusion causes mass flux to generate additional heat flux, promoting energy accumulation near the surface and deeper thermal penetration into the fluid. Figure 16 demonstrates that higher Df values amplify concentration overshoots and increase solutal boundary-layer thickness, reflecting stronger coupling between heat and mass diffusion. These results are consistent with previous studies [14, 16, 18, 28, 32].

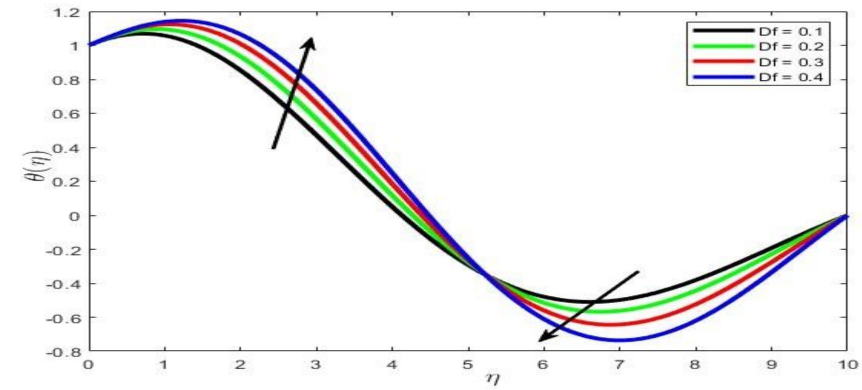

Figure 15: Effects of Df on Temperature Profiles

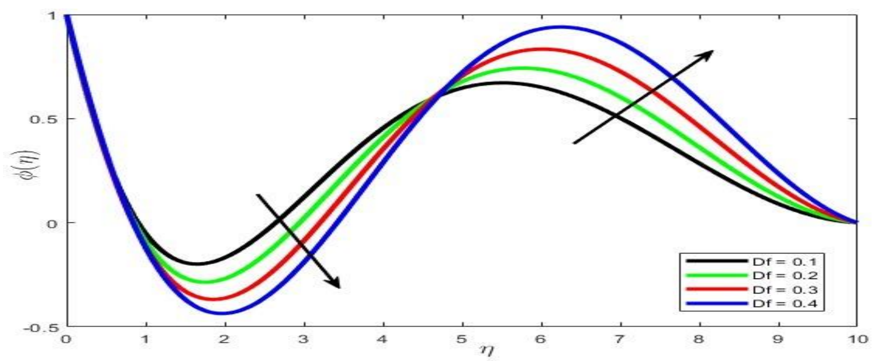

Figure 16: Effects of Df on Concentration Profiles

Effect of Schmidt Number

The impact of the Schmidt number Sc on the velocity, temperature, and concentration profiles are presented in Figures 17–19. As shown in Figure 17, increasing Sc suppresses the velocity distribution within the boundary layer. Higher Sc values correspond to lower mass diffusivity relative to momentum diffusivity, resulting in thinner hydrodynamic boundary layers and faster decay of velocity toward the free stream. This trend agrees with [18, 28].

Figure 18 illustrates that increasing Sc leads to a reduction in temperature across the boundary layer. Lower solutal diffusivity restricts energy transport, producing thinner thermal boundary layers and damping oscillatory temperature variations. Finally, Figure 19 shows that higher Sc values significantly reduce peak concentration levels and accelerate decay toward equilibrium. Reduced mass diffusivity limits solute transport, yielding thinner concentration boundary layers, consistent with observations reported in [14, 18, 28].

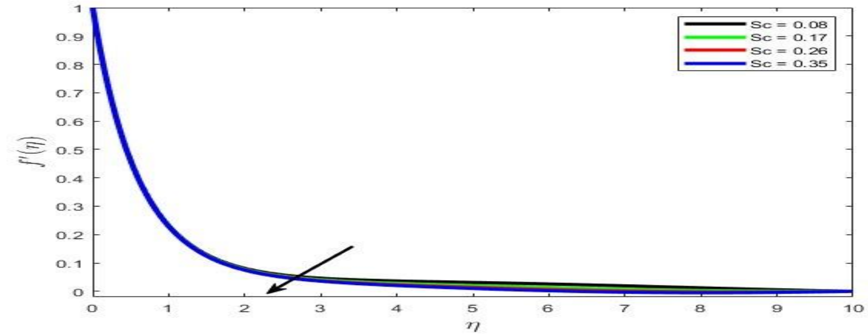

Figure 17: Effects of Sc Against Velocity Profiles

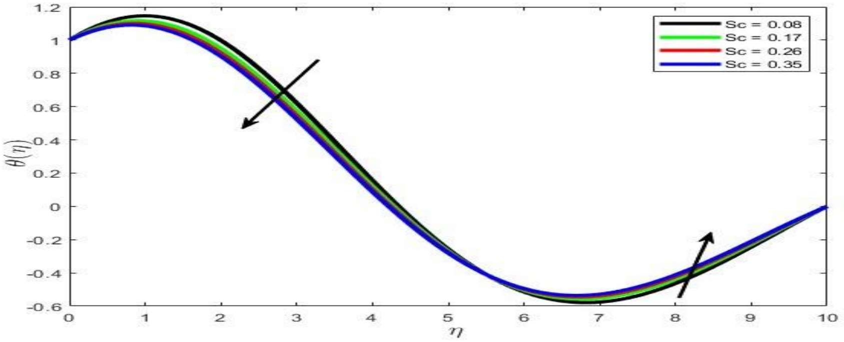

Figure 18: Effects of Sc Against Temperature Profiles

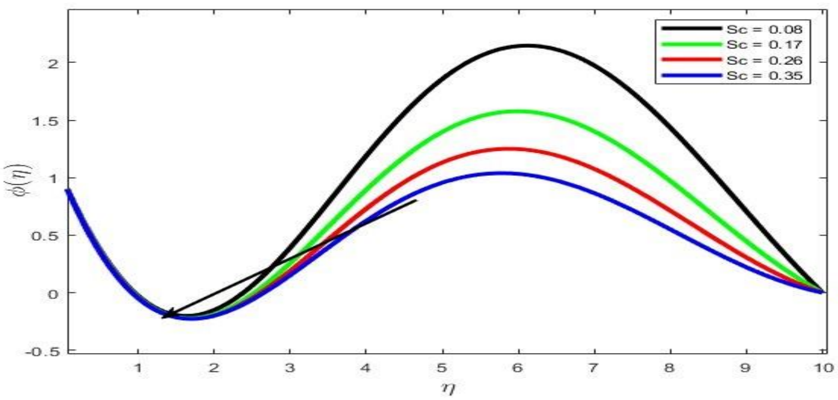

Figure 19: Effects of Sc against Concentration Profiles

CONCLUSION

The study highlights the combined influence of magnetic forces, nanoparticle transport, thermal–solutal interactions, reactive mass transfer, Casson MHD nanofluid flow over a linearly stretching sheet beneath a heat source/sink and radiative effects. The key findings can be summarised as follows:

i. Increasing M reduces fluid velocity while enhancing both temperature and concentration. This is attributed to Lorentz-force-induced resistance, which thickens the thermal and solutal boundary layers.
ii. A higher Nb has minimal impact on velocity but promotes thermal and mass diffusion, leading to

thinner boundary layers and diminishing mid-layer concentration peaks.

iii. Increasing Nt slightly suppresses near-wall velocity while significantly raising temperature and amplifying concentration gradients, leading to thicker thermal and solutal boundary layers.

iv. An increase in the chemical reaction parameter Kr weakens velocity, reduces temperature, and suppresses concentration peaks as stronger destructive reactions thin the momentum, thermal, and solutal boundary layers.

v. Increasing Df does not alter velocity but elevates temperature and enhances concentration overshoot by reinforcing cross-diffusion, thus thickening the thermal and solutal layers.

vi. Higher Sc decreases velocity, lowers temperature, and diminishes concentration peaks due to reduced mass diffusivity, producing uniformly thinner hydrodynamic, thermal, and solutal boundary layers.

The analysis delineates the dominant mechanisms controlling each aspect of the flow: magnetic forces primarily regulate the hydrodynamic field, nanoparticle dynamics, Brownian motion and thermophoresis govern energy and mass diffusion. Chemical reactions act as a uniform depletory of all boundary layers, whereas cross-diffusion via the Dufour effect strengthens thermal-solutal coupling. Notably, the Schmidt number emerges as a key stabilizing factor, significantly moderating all three boundary layers by restricting mass transport. These findings offer valuable insights for optimizing coupled heat and mass transfer processes in industrial and biomedical systems, including nanofluid-based cooling technologies and advanced reactor designs, by identifying which parameters most effectively control flow, thermal, and solutal behaviours.

Scientifically, this work provides the first combined quantification of Dufour-driven enhancement of wall heat transfer in Casson nanofluids under MHD and radiative effects for a linear stretching sheet, and demonstrates that Schmidt number variations can be used to simultaneously stabilize hydrodynamic, thermal and solutal boundary layers in reactive nanofluid flows. Future work will extend the present model to unsteady and three-dimensional configurations, include viscous and Joule dissipation, and pursue experimental validation for selected parameter ranges.

REFERENCES

Ajeeb, W., Murshed, S.M. (2023). Numerical Study of convective heat transfer performance, entropy generation and energy efficiency of Al and Al_2O_3 nanofluids in mini channel. *American Scientific Publishers, 12(1):18–28.* http://doi.org/10.1166/jon.2023.1903

Alreshidi, N.A., Shah, Z., Dawar, A., Kumam, P., Shutaywi, M., Watthayu, W. (2020). Brownian motion and thermophoresis effects on mhd three-dimensional nanofluid flow with slip conditions and Joule dissipation due to porous rotating disk. *Molecules, 25(3):729.* http://doi.org/10.3390/molecules25030729

Animasaun, I.L., Oyem, A.O. (2014). Effect of variable viscosity, dufour, soret and thermal conductivity on free convective heat and mass transfer of non-darcian flow past porous flat surface. *American Journal of Computational Mathematics, 4:357-365.* https://dx.doi.org/10.4236/ajcm.2014.44030

Ashraf, S., Mushtaq, M., Jabeen, K., Farid, S., Muntazir, R.M.A. (2023). Heat and mass transfer of unsteady mixed convection flow of casson fluid within the porous media under the influence of magnetic field over a nonlinear stretching sheet. *Proceedings of the Institution of Mechanical Engineers, Part C: Journal of Mechanical Engineering Science, 237(1).* https://doi.org/10.1177/09544062221110397

Asshaari, I., Shafie, S., Nazar, R. (2022). Brownian motion and thermophoresis effects in coflowing carbon nanotubes towards a moving plate. *Results in Physics, 40:106165.* https://doi.org/10.1016/j.rinp.2022.106165

Avinash, K., Reddy, R.H., Oyem, O.A. (2018). Analysis of mhd non-newtonian fluid over a stretching sheet with thermophoresis and Brownian moment. *Advanced Engineering Forum, 28:33–46.* https://dx.doi.org/10.4028/www.scientific.net/AEF.28.33

Beben-Kucharska, G.H.B, Mulka, R., Zajkaczkowski, B. (2025). Effect of axial and lateral magnetic field configurations on heat transfer in mixed convection ferrofluid flow. *Energies, 18(18):4790.* https://doi.org/10.3390/en18184790

Bulinda, V.M., Kangethe, G.P., Kiogora, P.R. (2020). Magnetohydrodynamics free convection flow of incompressible fluids over corrugated vibrating bottom surface with hall currents and heat and mass transfers. *Journal of Applied Mathematics, 3(20):1–10.* http://dx.doi.org/10.1155/2020/2589760

Buongiorno, J. (2006). Convective transport in nanofluids. *Journal of Heat Transfer, 128(3):240–250.* http://doi.org/10.1115/1.2150834

Dandu, S., Chitrapu, V.R.M., Kodi, R., et al., (2024). An investigation into the impact of thermal radiation and chemical reaction on oscillatory peristaltic Casson fluid flow in a porous medium. *Open Physics, 22:20240043.* https://doi.org/10.1515/phys-2024-0043

Deepika, A.R., Kamatam, G., Rana, A., Reza, M. (2023). Soret and Dufour effects on mhd mixed convection flow of Casson hybrid nanofluid over a permeable stretching sheet. International *Journal of Ambient Energy, 44(1):2115–2127*. https://doi.org/10.1080/01430750.2023.2224337

El-ashhab, A.G., Wahab, M.A., Hamza, S.E.E., Moatimid, G.M., Waheed, S.E. (2025). Effect of nanoparticle aggregation on casson nanofluid flow at a stagnation point with modification darcy model and entropy generation. *Discover Applied Sciences, 7*. https://doi.org/10.1007/s42452-025-07701-8

Faraz, F., Imran, S.M., Ali, B., Haider, S. (2019). Thermo-diffusion and multi-slip effect on an axisymmetric Casson flow over an unsteady radially stretching sheet in the presence of chemical reaction. *Processes, 7(11):851*. https://doi.org/10.3390/pr7110851

Filahi, I., Bourich, M., Hasnaoui, M., Amahmid, A. (2020). Analytical and numerical study of Soret and Dufour effects on thermosolutal convection in a horizontal Brinkman porous layer with a stress-free upper boundary. *Mathematical Problems in Engineering, 17: Article ID 4046570*. https://doi.org/10.1155/2020/4046570

Goyal, M., Bhargava, R. (2013). Boundary layer flow and heat transfer of viscoelastic nanofluids past a stretching sheet with partial slip conditions. *Applied Nanoscience, 4(6):761–767*. https://doi.org/10.1007/s13204-013-0254-5

Hussain, A., Raiz, S., Hassan, A., Hassan, A.M., Karamti, H., Bogn´ar, G. (2024). Analysis of Soret and Dufour effects on radiative heat transfer in hybrid bioconvective flow of carbon nanotubes. *Scientific Reports, 14(1): Article 11970*. https://doi.org/10.1038/s41598-024-62647-2

Hussain, M., Fatima, S., Qayyum, M. (2024). Radiative mixed convection flow of casson nanofluid through exponentially permeable stretching sheet with internal heat generation. *Journal of Mathematics, 2:1–12*. https://doi.org/10.1155/2024/9038635

Idowu, A.S., Falodun, B.O. (2019). Soret–Dufour effects on mhd heat and mass transfer of Walter's-B viscoelastic fluid over a semi-infinite vertical plate: Spectral relaxation analysis. *Journal of Taibah University for Science, 13(1):49–62*. https://doi.org/10.1080/16583655.2018.1523527

Islam, M.R., Reza-E-Rabbi, S., Ali, M.Y., Hasan Rasel, M., Ahmmed, S.F. (2023). Numerical simulation of mass and heat transport phenomena of hydromagnetic flow of Casson fluid with sinusoidal boundary conditions. *Engineering Reports*. https://doi.org/10.1002/eng2.12659

Jaffrullah, S., Sridhar, W., Ganesh, G.R. (2024). Analysis of mhd casson nanofluid flow over a nonlinearly stretching surface with Joule heating, radiation and suction effects. *International Journal of Heat and Technology, 2(42):414–426*. https://doi.org/10.18280/ijht.420207

Khan, M.S., Mei, S., Guled, C., Abdollahzadeh, M. (2022). Effects of thermophoresis and Brownian motion for thermal and chemically reacting Casson nanofluid flow over a linearly stretching sheet. *Results in Engineering, 15:100448*. https://doi.org/10.1016/j.rineng.2022.100448

Kigio, J.K., Winifred, N.M., Oke, A.S. (2021). Analysis of volume fraction and convective heat transfer on mhd casson nanofluid over a vertical plate. *Fluid Mechanics, 7(1):1–8*. http://dx.doi.org/10.11648/j.fm.20210701.11

Kodi, R., Mohana Ramana, R., Ramachandra R.V., Obulesu, M. (2023). Diffusion thermo and chemical reaction effects on magnetohydrodynamic Jeffrey nanofluid over an inclined vertical plate in the presence of radiation absorption and constant heat source. *Journal of Nanofluids, 12(1):147-156*. https://doi.org/10.1166/jon.2023192325

Koriko, O.K., Oreyeni, T., Oyem, O.A. (2018). On the analysis of variable thermophysical properties of thermophoretic viscoelastic fluid flow past a vertical surface with nth order of chemical reaction. *Open Access Library Journal, 5- e4271:1–17*. https://dx.doi.org/10.4236/oalib.1104271

Krishnamurthy, M.R., Prasannakumara, B.C., Gireesha, B.J., Gorla, R.S.R. (2015). Effect of chemical reaction on MHD boundary layer flow and melting heat transfer of Williamson nanofluid in porous medium. *Engineering Science and Technology, an International Journal, 19(1):53–61*. https://doi.org/10.1016/j.jestch.2015.06.010

Kumar, M., Srinivasa, R., Mebarek-Oudina, F., Anil Kumar, M., Narla, V.K. (2024). Cross-diffusion effects on an mhd Williamson nanofluid flow past a nonlinear stretching sheet immersed in a permeable medium. *Frontiers in Heat and Mass Transfer, 22(1):15–34*. https://doi.org/10.32604/fhmt.2024.048045

Kune, R., Naik, H.S., Reddy, B.S., Chesneau, C. (2022). Role of nanoparticles and heat source/sink on mhd flow of Cu–H2O casson nanofluid past a vertical plate with soret and dufour effects. *Mathematics and Computers in Simulation, 27(6)*. https://doi.org/10.3390/mca27060102

Manthramurthy, P., and Rao, S. (2024). Thermophoresis and Soret-Dufour on mhd mixed convection of a nano Fluid with a porous medium over a stretching sheet with a non-uniform heat source/sink. *International Journal of Applied Mathematics and Theoretical Physics, 10(1):1-20*. https://doi.org/10.11648/j.ijamtp.20241001.11

Misra, S., Kamatam, G. (2020). Effect of magnetic field, heat generation and absorption on nanofluid flow over a nonlinear stretching sheet. *Beilstein Journal of Nanotechnology, 11:976–990*. https://doi.org/10.3762/bjnano.11.82

Muhammad, M.Y., Lawan, M.A., Gambo, Y.Y. (2024). Heat absorption effect of magneto-natural convection flow in vertical concentric annuli with influence of radial and induced magnetic field. *Scientific Reports, 14:15165*. https://doi.org/10.1038/s41598-024-64779-x

Nadeem, M., Siddique, I., Saif-Ud-Din, I., Awwad, F.A.A., Ismail, E.A.A., Ahmad, H. (2023). Impact of chemical reaction on Eyring–Powell fluid flow over a thin needle with nonlinear thermal radiation. *Scientific Reports, 13: Article 21401*. https://doi.org/10.1038/s41598-023-48400-1

Nagari, H.C., Firdi, M.D., Rikitu, E.H. (2025). Analyzing Soret and Dufour effects on mhd variable viscosity casson nanofluid flow past a stretching sheet with heat source/sink. *Advances in Mathematical Physics, 1–22*. https://doi.org/10.1155/admp/2167629

Onojovwo, F.T., Oyem, O.A., Momoh, S.O., Sheid, A.M. (2023). Casson nanofluid flow over a vertical plate and its thermophysical properties. *FUW Trends in Science and Technology Journal, 8(2):044–052*. www.ftdtjournal.com

Oyekunle, T.L., Akolade, M.T., Agunbiade, S.A., Adeniran, P.O. (2023). MHD stagnation point flow of nanofluid with buoyancy effect through a porous shrinking sheet. *Applications and Applied Mathematics: An International Journal, 19(1): Article 7*. https://digitalcommons.pvamu.edu/aam/vol19/iss1/7

Oyem, O.A., 2015. Effects of thermophysical properties on free convective heat and mass transfer flow over a vertical plate. *Unpublished PhD Thesis, Federal University of Technology Akure, Nigeria*.

Patil, P.M., Salunke, N.J., Salunke, J.N. (2017). Nanofluid under uniform transverse magnetic field with a chemical reaction past a stretching sheet. *arXiv:1712.09421*. https://arxiv.org/abs/1712.0942124

Ramasekhar, G., Hamdard, L., Hadi, A., Jawad, M., Gull, H., Zashan, M. (2026). Analysis of non-newtonian fluid

Ramudu, A.C.V., Kumar, K.A., Sugunamma, V., Sandeep, N. (2020). Heat and mass transfer in mhd casson nanofluid flow past a stretching sheet with thermophoresis and Brownian motion. *Heat Transfer*. https://doi.org/10.1002/htj.21865

Ramya, R.N. Deivanayaki, M. (2025). Impact of soret and dufour effects on casson nanofluid flow in a magnetic field along with heat and mass transfer. Indian Journal of Science and Technology, *18(13):1059-1070*. https://doi.org/10.17485/IJST/v18i13.4028

Ramzan, M., Khan, M.I., et. al. (2023). A theoretical analysis of the ternary hybrid nanofluid flows over non-isothermal and non-isosolutal multiple geometries. Heliyon, *9: Article e14875*. https://doi.org/10.1016/j.heliyon.2023.e14875

Ramzan, M., Khan, N.S., Kumam, P., Khan, R., et. al. (2021). A numerical study of chemical reactions in a nanofluid flow due to rotating disk in the presence of magnetic field. *Scientific Reports, 11: Article 19399*. https://doi.org/10.1038/s41598021-98881-1

Reddy, B., Shashidar, Reddy, B., Narsimha, Saritha, K., Chesneau, C. (2025). MHD hyperbolic-tangent Casson–Williamson nanofluid over a linearly stretching sheet with thermophoresis and Brownian motion. *International Journal of Applied Mechanics and Engineering, 30(2):124–139*. https://doi.org/10.59441/ijame/200965

Sademaki, L.J., Reddy, B.P., Matao, P.M., (2025). Thermophoresis and Brownian motion impact on diffusional heat-generating MHD Jeffrey nanofluid over an inclined vertical cone with reactive species *Discover Applied Sciences, 7(10):* http://doi.org/10.1007/s42452-025-06840-6

Seid, E., Haile, E., Walelign, T. (2024). Induced magnetic field and Soret–Dufour effects on viscous dissipative Casson fluid flow over a stretching sheet. *Journal of Thermal Analysis and Calorimetry*. https://doi.org/10.1007/s10973-02413352-9

Sohail, M., Rafique, E., Singh, A., Tulu, A. (2024). Engagement of modified heat and mass fluxes on thermally radiated boundary layer flow past over a stretched sheet via OHAM analysis. *Discover Applied*

Sciences, 6:240. https://doi.org/10.1007/s42452-024-05833-1

Sudarsana R.P., Sreedevi, P., Chamkha, A.J. (2018). Magnetohydrodynamic (MHD) boundary layer heat and mass transfer characteristics of nanofluid over a vertical cone under convective boundary condition. *Propulsion and Power Research, 7(4):308–319*. https://doi.org/10.1016/j.jppr.2018.11.004

Tawade, J.V., Guled, C.N., Noeiaghdam, S., Fernandez-Gamiz, U., Govindan, V., Balamuralitharan, S. (2022). Effects of thermophoresis and Brownian motion for thermal and chemically reacting Casson nanofluid flow over a linearly stretching sheet. *Results in Engineering, 15:100448*. https://doi.org/10.1016/j.rineng.2022.100448

Tejaswini, G.K., Vinutha, K., Madhukesh, J.K., Reddy, P.S.K., Khan, U., 2026. RKF45 optimization for the boundary layer hybrid nanofluid flows of stationary and moving flat plates with chemical reactions. *Discover Applied Sciences, 8*. https://doi.org/10.100.1007/s42452-026-08388-5

Ullah, H., Abas, S.A., Fiza, M., Khan, I., Rahimzai, A.A., Akgul, A. (2024). A numerical study of heat and mass transfer characteristic of three-dimensional thermally radiated bi-directional slip flow over a permeable stretching surface. *Scientific Reports, 14: Article 19842*. https://doi.org/10.1038/s41598-024-70167-2

Upadhya, S.M., Raju, C.S.K., Vajravelu, K., Guinovart-Sanju´an, D. (2023). Analysis of micro-hybrid and casson-hybrid nano-convective and radiative fluid flow in an inclined channel. *Journal of Nanofluids, 12(1):104–114*. https://doi.org/10.1166/jon.2023.1916

Vaishnav, B.K., Choudhary, S., Choudhary, P., Jat, K., Loganathan, K., Eswaramoorthi, S. (2025). Computational analysis of radiative micropolar fluid flow over a curved stretching sheet with viscous dissipation. *Discover Applied Sciences, 7:451*. https://doi.org/10.1007/s42452-025-06983-6

Venkateswarlu, B., Satya Narayana, P.V. (2015). Chemical reaction and radiation absorption effects on the flow and heat transfer of a nanofluid in a rotating system. *Applied Nanoscience, 5(3):351-360*. https://doi.org/10.1007/s13204-0140324-3

Williams, M., Yabo, I. (2024). The upshots of dufour and soret in stretching porous flow of convective Maxwell nanofluid with nonlinear thermal emission. *International Journal of Theoretical and Applied Mathematics, 10(3):38-50*. https://doi.org/10.11648/j.ijtam.20241003.12

Yacob, N.A., Ishak, A., Pop, I., Vajravelu, K. (2011). Boundary layer flow past a stretching/shrinking surface beneath an external uniform shear flow with a convective surface boundary condition in a nanofluid. *Nanoscale Research Letters, 6(1)*. https://dx.doi.org/10.1186/1556-276x-6-314

Yang, H., Majeed, A., Al-Khaled, K., Abbas, T., Naeem, M., Khan, S.U., Saeed, M. (2023). Significance of melting heat transfer and brownian motion on flow of Powell–Eyring fluid conveying nano-sized particles with improved energy systems. *Lubricants, 11(1)*. http://doi.org/10.3390/lubricants11010032

Zuberi, H.A., Lal, M., Verma, S., Zainal, N.A. (2024). Computational investigation of brownian motion and thermophoresis effect on blood-based Casson nanofluid on a non-linearly stretching sheet with ohmic and viscous dissipation effects. *Computer Modeling in Engineering and Sciences, 141(2):1137–1163*. https://doi.org/10.32604/cmes.2024.055493